minerals

MDPI

Article

Significance of Secondary Fe-Oxide and Fe-Sulfide Minerals in Upper Peak Ring Suevite from the Chicxulub Impact Structure

Christina M. Verhagen [1], Ji-In Jung [2], Sonia M. Tikoo [2,3,*], Axel Wittmann [4], David A. Kring [5], Stefanie Brachfeld [6], Laying Wu [6], Dale H. Burns [3] and Sean P. S. Gulick [7,8]

1 Department of Earth and Planetary Sciences, Rutgers University New Brunswick, Piscataway Township, NJ 08854, USA
2 Department of Geophysics, Stanford University, Stanford, CA 94305, USA
3 Department of Geological Sciences, Stanford University, Stanford, CA 94305, USA
4 Eyring Materials Center, Arizona State University, Tempe, AZ 85287, USA
5 Lunar and Planetary Institute, Houston, TX 77058, USA
6 Department of Earth and Environmental Sciences, Montclair State University, Montclair, NJ 07043, USA
7 Institute for Geophysics and Department of Geological Sciences, Jackson School of Geosciences, University of Texas at Austin, Austin, TX 78712, USA
8 Center for Planetary Systems Habitability, University of Texas at Austin, Austin, TX 78712, USA
* Correspondence: smtikoo@stanford.edu

Abstract: The suevite (polymict melt rock-bearing breccia) composing the upper peak ring of the Chicxulub impact crater is extremely heterogeneous, containing a combination of relict clasts and secondary minerals. Using scanning electron microscopy coupled with energy-dispersive X-ray spectroscopy (SEM/EDS) and electron probe microanalysis (EPMA), we investigated the nature and occurrence of primary and secondary Fe-oxide and Fe-sulfide minerals to better understand hydrothermal trends such as mineral precipitation and dissolution, and to document the remobilization of Fe and associated siderophile elements within suevites. Large primary Fe-oxides (~20–100 µm) reveal decomposition and dissolution patterns, forming sub-micrometer to micrometer Fe-oxide phases. Secondary sub-micrometer Fe-oxide crystals are also visibly concentrated within clay. The occurrence of Fe-oxide crystals within clay suggests that these likely formed at temperatures ≤100 °C, near the formation temperature of smectite. The formation of Fe-oxide minerals on clay surfaces is of interest as it may form a micro-setting, where free electrons (from the oxidation of Fe^{2+}) and the adsorption of simple organic molecules on the surface of clay could generate reactive conditions favorable to microbial communities. Primary and secondary Fe-sulfide minerals exhibiting a variety of morphologies are present within samples, representing different formation mechanisms. Secondary Fe-sulfide minerals occur within rims of clasts and vesicles and in fractures and voids. Some secondary Fe-sulfide grains are associated with Ni- and Co-rich phases, potentially reflecting the post-impact migration of siderophile elements within the suevite of the Chicxulub crater.

Keywords: hydrothermalism; impact cratering; suevite; Fe-oxide minerals; Fe-sulfide minerals

Citation: Verhagen, C.M.; Jung, J.-I.; Tikoo, S.M.; Wittmann, A.; Kring, D.A.; Brachfeld, S.; Wu, L.; Burns, D.H.; Gulick, S.P.S. Significance of Secondary Fe-Oxide and Fe-Sulfide Minerals in Upper Peak Ring Suevite from the Chicxulub Impact Structure. *Minerals* **2023**, *13*, 353. https://doi.org/10.3390/min13030353

Academic Editors: Alexander R Cruden and Roman Skála

Received: 1 December 2022
Revised: 24 February 2023
Accepted: 28 February 2023
Published: 2 March 2023

1. Introduction

Within an impact crater, residual heat from uplifted basement rocks and protracted cooling of impact melt rocks can drive fluid migration through pore spaces and fractures for potentially millions of years [1–7]. Hydrothermal fluids leach elemental nutrients, including iron (Fe), from the rocks they permeate. Oxidation of Fe can increase redox gradients in circulating fluids which may be useful for generating an environment hospitable for life [8,9] in the impact crater rocks. For the aforementioned reasons, it has been hypothesized that life on Earth may have originated or been nurtured in a hydrothermal system generated by an impact event [10–14]. By analyzing hydrothermal minerals precipitated within impact crater rocks, we can better understand the chemical conditions of a

hydrothermal environment and how those conditions may support the recovery of life in a crater setting or even the origin of life on a planet. Results can then be useful to ongoing astrobiological studies.

Secondary minerals precipitated from hydrothermal fluids can be useful for fingerprinting chemical conditions within post-impact hydrothermal systems [15]. In addition, the spatial relationships between secondary mineral assemblages and surrounding mineral phases can be used to constrain the formation temperatures of secondary minerals. Specifically, Fe-rich secondary minerals such as magnetite and Fe-sulfides are of interest. Fe^{2+} is oxidized to Fe^{3+} in the formation of magnetite (Fe_3O_4), generating free electrons. Secondary magnetite can acquire chemical remanent magnetization (CRM), recording the Earth's magnetic field direction and intensity at the time that it precipitates [16]. Several works have proposed that remanent magnetization within hydrothermally precipitated magnetite grains in crater rocks may record reversals of the Earth's magnetic field if magnetite formation continues through a geomagnetic reversal [1,17–19]. The documentation of reversals within crater rocks can potentially provide a dating mechanism for the duration of hydrothermalism within a crater.

Highly siderophile elements (e.g., Re and Au), including the platinum group elements (PGE; e.g., Os, Ir, Ru, Pt, Rh and Pd), are used to identify material from an impact projectile [20,21]. Moderately siderophile elements (Ni, Co, Cu) often associated with sulfide minerals are known to produce economic deposits within impact craters. Impact melting at the Sudbury impact structure in Canada generated an opportunity for crustal Ni and PGEs to be concentrated at the base of the impact melt sheet, in offset dikes, and remobilized in hydrothermal deposits, forming economic deposits [22]. The Vredefort impact structure in South Africa is thought to have contained similar economic deposits to Sudbury but has eroded below these depths [23]. The Chicxulub impact structure, Yucatán Peninsula, México, is a well-studied multi-ring crater, linked to the Cretaceous–Paleogene mass extinction event [20,24–26]. Drill cores collected from the annular trough of the Chicxulub crater (e.g., Yaxcopoil-1, Yucatán 6) were examined for PGE abundances. X-ray fluorescence (XRF) spectroscopy and inductively coupled plasma mass spectrometer (ICP-MS) analyses of these cores determined that the concentration of PGEs in impact melt and suevite (impact breccias containing impact melt fragments) resembled that of continental crust and any meteoritic fraction was below 0.05% [27,28]. However, we note that because these cores only sampled the uppermost annular trough, the PGE concentration of deeper regions within the annular trough or the crater's central melt sheet could differ.

In 2016 the International Ocean Discovery Program (IODP) and International Continental Scientific Drilling Program (ICDP) Expedition 364 drilled into the peak ring of the Chicxulub crater, recovering 829 m of drill core from 505.7 to 1334.7 m below sea floor (mbsf) [25,29] at Hole M0077A. The core contains uplifted granitoid rocks capped by impact melt rocks, suevite, and post-impact sedimentary rocks [29] (Figure 1). The entire core shows evidence of hydrothermal alteration. However, the highly porous rocks of the suevite section have been extensively hydrothermally altered [1,30]. While the Chicxulub impact structure is not yet known to contain economic deposits, nor a significant incorporation of meteoritic material [28,31], it does contain siderophile elements incorporated from mafic target rocks, possibly pre-impact dolerite dikes that crosscut the felsic basement [31]. Feignon et al. [31] used petrographic investigations to show that the impact melt rocks in M0077A reflect mixing of felsic (granite) and mafic (dolerite) target lithologies. However, moderately siderophile elements such as Ni and Co may have been redistributed throughout the upper peak ring sequence, explaining features of the samples they analyzed, such as relatively low amounts of Cr, Co, and Ni within the basement granite compared to upper continental crust (UCC) values. The effects of post-impact hydrothermal alteration may account for remobilization of these elements and reincorporation of them especially within sulfide phases. However, it has not been well documented how these elements are remobilized by hydrothermalism within Chicxulub suevite. Moreover, while Fe-oxide minerals (e.g., magnetite) and Fe-sulfide minerals (e.g., pyrite, chalcopyrite, framboidal

pyrite, Ni-bearing pyrite, Fe-Co-Ni-Cu sulfide) have been documented in suevite and impact melt rock samples from Hole M0077A (supplementary materials from [1]), no study to date has yet focused in detail on the occurrence of both primary and secondary minerals which contain siderophile elements within the suevite sequence. For these reasons, we employed petrographic imaging as well as qualitative and quantitative elemental analyses to locate and document Fe-oxide and Fe-sulfide minerals within suevite samples.

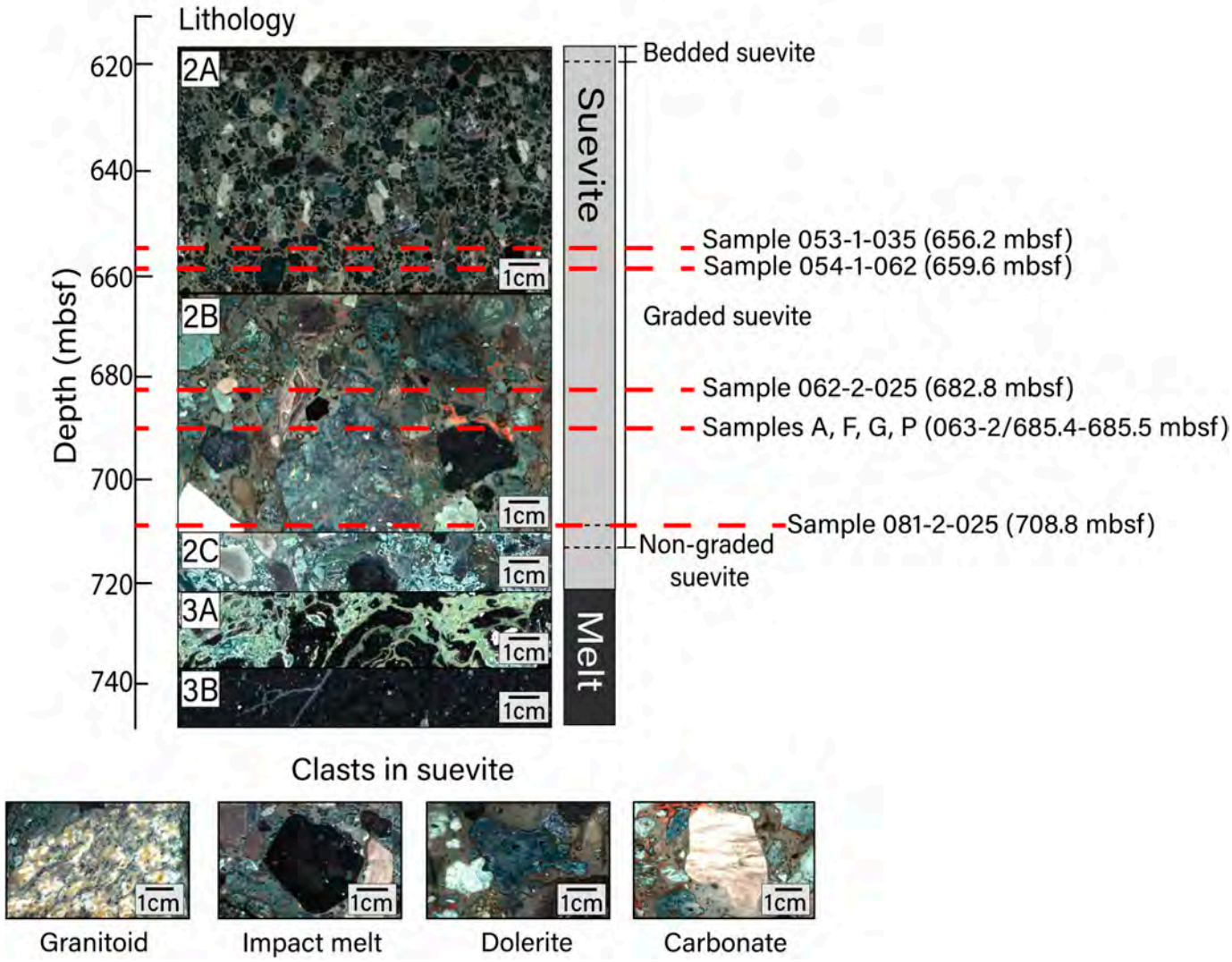

Figure 1. Upper peak ring lithological units with depth. Unit 2 is composed of suevite and is divided into subunits 2A (617.22–664.52 mbsf; image from core section 53-1), 2B (664.52–712.83 mbsf; image from core section 67-1), and 2C (712.83–721.62 mbsf; image from core section 84-2). Unit 2 is further divided into bedded, graded, and non-graded suevite. Unit 3 is composed of impact melt rocks and is divided into subunits 3A (721.62–737.56 mbsf; image from core section 88-4) and 3B (737.56–747.02 mbsf; image from core section 95-1). Subunit depth boundaries are defined in [32]. Representative images of clast types within the suevite include (sample name/sample depth in mbsf) granitoid (081-3-007/710.06 mbsf), impact melt (081-3-020/710.19 mbsf), dolerite (066-1-022/689.58 mbsf), and carbonate (063-3-008/686.07 mbsf) lithologies. Thin sections for this study were prepared for samples at the depths noted. All images shown in this figure are macroscopic digital line scan photos that were obtained from drill core archive halves during the Expedition 364 Onshore Science Party. All line scan images from Expedition 364 are publicly available and were obtained from the Bremen Core Repository curatorial database (doi:10.1594/PANGAEA.881718 (accessed on 17 February 2023)).

2. Materials and Methods

Suevite samples were recovered from between 617.33 and 712.83 mbsf at Hole M0077A. The suevite sequence is divided into subunits 2A–2C. Subunit 2C contains basement and carbonate clasts as well as an abundance of impact melt clasts and is thought to have formed when a resurge of seawater flooded the newly formed crater, explosively interacting with the impact-melted rocks below [33–35]. Subunits 2B and 2A were deposited during the continued return of seawater to the crater [33,34]. Coarse-grained, clast-supported subunit 2B generally fines upward into the fine–medium-grained, matrix-supported subunit 2A [32]. All subunits display hydrothermal alteration including an abundance of clay; degassing pipes are documented in the upper portion of the suevite [1,30,32]. Simpson et al. [30] analyzed the varieties of clay using EPMA and powder X-ray diffraction, determining that subunit 2A contains saponite (trioctahedral Mg-Fe smectite) and that certain regions within subunit 2B (between 686 and 708 mbsf) contain an assemblage of dioctahedral, Al-rich smectite group minerals. In accordance with this prior work, we hereafter refer to the relevant clay mineral occurrences in subunit 2A as saponite (Sap) and those within subunit 2B as smectite. Hydrothermally altered zones include secondary calcite, clays, analcime, and dachiardite-Na, as well as Fe-oxide and Fe-sulfide minerals interpreted to be of hydrothermal origin. Suevite subunit 2B is particularly heterogeneous, containing primary clasts from target granitoid and carbonate rocks as well as fragments of impact melt rocks within a matrix that contains a K-rich feldspathic (anorthoclase-like) phase, a SiO_2 phase, and a less dominant carbonate component. Portions of subunit 2B also contain fragments of altered solidified impact melt. Previous efforts to determine the composition of Chicxulub impact melt rocks have been made on drill cores Chicxulub-1 (C1) and Yucatan-6 (Y6) as well as the one obtained from Hole M0077A [36–38]. Impact melt materials from Hole M0077A have trachyandesite or trachyte-like compositions; this compositional range is broadly consistent with that inferred for impact melt rocks from other sites within the crater [37].

We prepared thin sections from subunit 2A cores 53R (656.24 mbsf) and 54R1 (659.56 mbsf) and subunit 2B cores 62R2 (682.84 mbsf) and 81R2 (708.78 mbsf). One thin section was prepared from each location from residues. Each of these thin sections was oriented parallel to the saw-cut faces of the split cores. In addition, we sliced a 10 cm piece of subunit 2B suevite (core 63R2/685.36–685.46 mbsf) into 16 square prisms ~1.75 cm on edge and 0.5 cm in height, labeled samples A–P, and made thin sections of each slice (Figure 1). To maximize available surface area, these thin sections were oriented perpendicular to the drill core. We first analyzed the thin sections using a reflected light microscope to identify areas that likely contained Fe-oxide and/or Fe-sulfide minerals. After identifying areas of interest, we studied the samples using scanning electron microscopy (SEM) at Montclair State University and/or Stanford University. At Montclair State, we used a Hitachi S-3400N SEM to generate backscattered electron (BSE) images using an acceleration voltage of 15 keV. Selected grains were analyzed via energy-dispersive X-ray spectroscopy (EDS) using a Bruker AXS X-flash X-ray detector, with a counting time of 60 s, to define elemental abundances.

Further quantitative SEM-EDS work was conducted at the Stanford University Microchemical Analysis Facility using a JEOL JSM-IT500HR SEM equipped with a Thermo Scientific UltraDry EDS spectrometer. At Stanford, grains were analyzed using an acceleration voltage of either 8 keV or 20 keV using a focused scanning electron beam. Scanned areas and conditions were kept consistent throughout the analytical session (1 μm × 1 μm area and 30 s frame time). EDS spectra were processed using the Thermo Scientific Pathfinder X-ray microanalysis software. Major element concentrations were calculated by comparing X-ray intensities from specific regions of interest (i.e., the energy range surrounding the X-ray peak or peaks of interest) in our unknown samples to similar regions in pure metals or stoichiometric synthetic oxide standards. To analyze Fe-oxides, we focused on the following elements (with corresponding X-ray lines/calibrants): Fe (Lα, Lβ/Fe metal), Ti (Kα/Ti metal), Al (Kα/Al_2O_3), Si (Kα/SiO_2), O (Kα/SiO_2). Peak-fitting and background radiation corrections were achieved using the top-hat filtering technique integrated into

the Pathfinder software. In all cases, peak deconvolutions were run to remove carbon from the spectra. Once standard to unknown X-ray intensity ratios were determined (i.e., k-ratios), quantitative matrix corrections were performed using the ZAF correction scheme [39]. In-run accuracy and reproducibility were determined and monitored using a well-characterized magnetite standard from the Smithsonian microbeam standards collection (NMNH 114887).

We further quantified the elemental abundances of specific Fe-oxide and Fe-sulfide crystals with wavelength dispersive spectroscopy (WDS) using a JEOL JXA-8230 SuperProbe electron microprobe at Stanford University. For WDS analyses, we used an accelerating voltage of 20 keV, a beam current of 20 nA, a focused spot size of 1 μm, and peak counting times of 20 s (10 s for Ba and Sr). The elements measured (and calibration standards used) were S (pyrite), Ti (TiO_2), Ca (wollastonite), Al (chromite), Mg (chromite), Si (wollastonite), Mn (spessartine), Cu (copper metal), Ba (barite), Cr (chromite), Fe (magnetite), Ni (Ni_2Si), V (vanadium metal), and Co (cobalt metal). EPMA detection limits were 0.02 wt.% for S, 0.02 wt.% for Ti, 0.01 wt.% for Ca, 0.01 wt.% for Al, 0.01 wt.% for Mg, 0.01 wt.% for Si, 0.03 wt.% for Mn, 0.04 wt.% for Cu, 0.05 wt.% for Ba, 0.02 wt.% for Cr, 0.01 wt.% for Fe, 0.01 wt.% for Ni, 0.02 wt.% for V, and 0.01 wt.% for Co.

We analyzed samples (sample name/depth in mbsf) 053-1-035/656.2 mbsf, 054-1-062/659.6 mbsf, 062-2-025/682.8 mbsf, and 081-2-025/708.8 mbsf as well as samples A/~685.4 mbsf, F/~685.42 mbsf, G/~685.43 mbsf, and P/~685.5 mbsf from the 10 cm long suevite block from core 63R2 which all contained Fe-oxide and Fe-sulfide minerals including identifiable secondary phases. Mineral phases were identified on the basis of chemical composition and stoichiometry rather than X-ray diffraction or Raman analyses. For Fe-oxide grains, the respective abundances of FeO and Fe_2O_3 were calculated using the approach of Carmichael [40] for both quantitative EDS and WDS data.

During SEM imaging, we sometimes noted occurrences of sub-micrometer Fe-rich grains within polishing debris. Such debris was observed within epoxy bubbles, along sample edges, and within pits. In Figure 2, we include both BSE and secondary electron (SE) images to show artifacts of polishing and topographic features that imply contamination, such as particles lying on top of the thin section or grains with a shard-like appearance. To ensure that the features we report below as Fe-oxides and Fe-sulfides were intrinsic to samples (and not contamination), we excluded reporting grains that occurred within material that resembled polishing debris in both BSE and SE imagery as well as grains that were located close to sample edges.

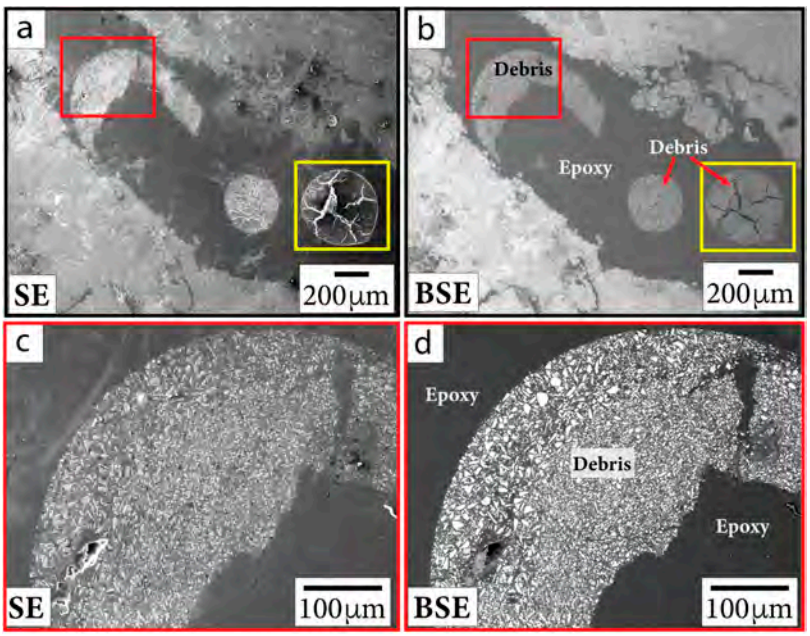

Figure 2. *Cont.*

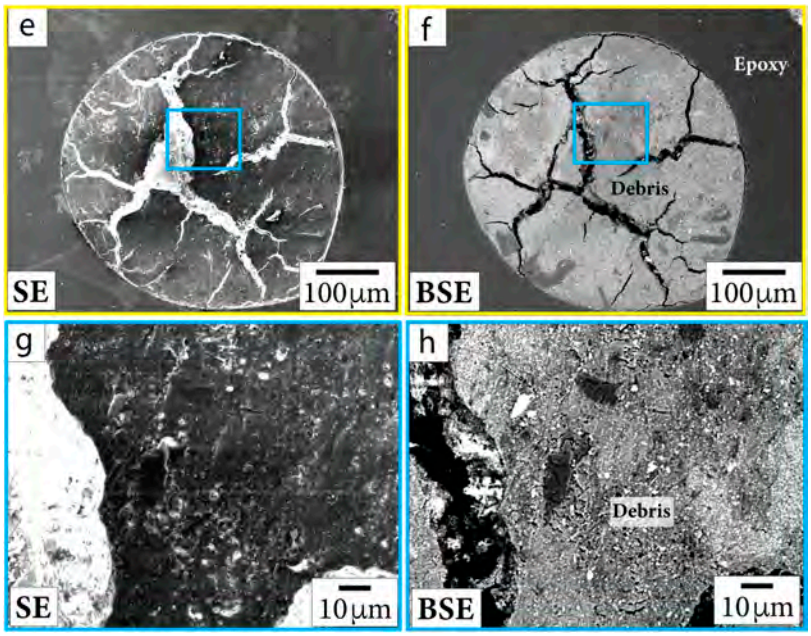

Figure 2. SE (first column) and BSE (second column) images of polishing debris in sample P/~685.5 mbsf. Close-up images (**c**–**h**) are outlined in the same color as the boxes shown in context images (**a**,**b**,**e**,**f**). Debris is documented in bubbles in epoxy and in thin section material near the edges of the sample.

3. Results

The suevite contains several Fe-oxide and Fe-sulfide minerals, and it is often difficult to interpret their origin. We utilized a tree chart to categorize the composition and occurrence of Fe-oxide and Fe-sulfide minerals. These factors help in identifying whether a mineral is primary or secondary (Figure 3).

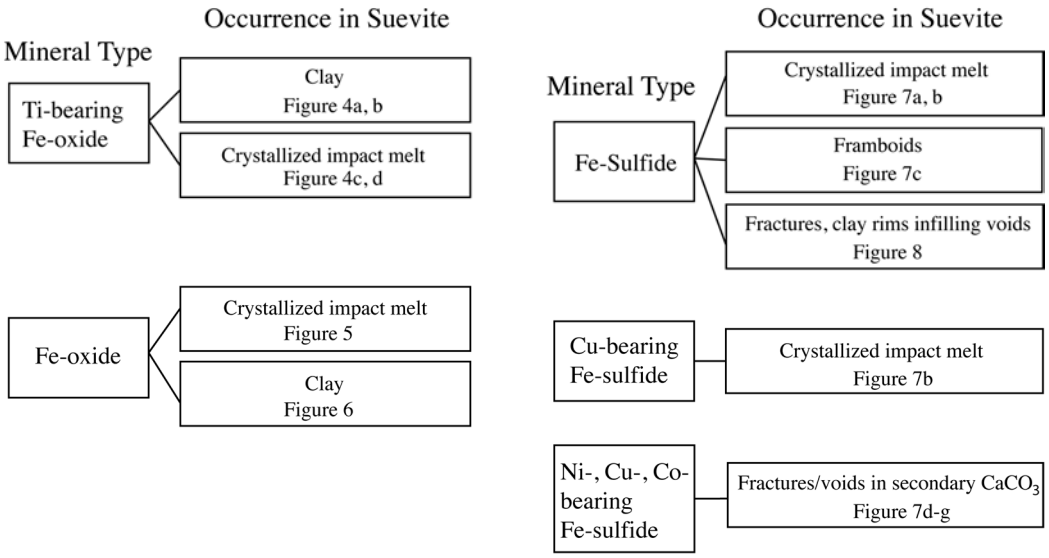

Figure 3. Tree chart utilized to describe compositions and occurrences of Fe-oxide and Fe-sulfide minerals in suevite samples. Figures corresponding to each occurrence mode are noted in the chart.

3.1. Occurrences of Fe-Oxide Grains

Primary Fe-oxide minerals (sourced from target rocks) are the most easily identifiable. These grains are large (~20–100 μm), often include titanium (Ti), and show evidence of microfracturing from shock (Figure 4). Quantitative EDS and WDS analyses collectively

suggest these grains are likely composed of Ti-bearing magnetite (Tables 1 and 2). Some Ti-bearing magnetite grains, particularly within sample G/~685.43 mbsf, are associated with TiO_2 at their peripheries and appear to have Ti-rich exsolution lamellae within the grains. This additional Ti produces a lower value of $Fe^{3+}/\sum Fe$ than expected for pure magnetite (0.67) in quantitative EDS analyses. These Fe-oxide minerals often appear to be altered and decomposed, especially along fractures within grains and at the peripheries of grains.

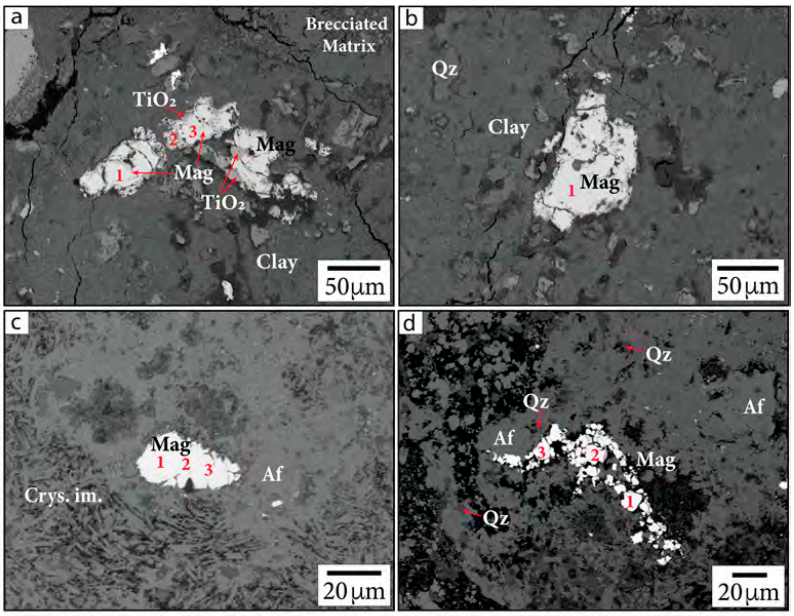

Figure 4. Primary Fe-oxide phases in BSE images. (**a**,**b**) Sample G/~685.43 mbsf; (**c**,**d**) sample P/~685.5 mbsf. Samples are identified in the following format: sample name/depth in mbsf. Numbers indicate locations of calibrated quantitative EDS analyses. Mag = magnetite, Crys. im. = crystallized impact melt, Qz = quartz. Af = alkali feldspar group minerals, following the nomenclature of [37].

Table 1. Calibrated quantitative EDS analyses of Fe-oxide and mixed oxide phases (oxide wt.%) from sample G/~685.43 mbsf and sample P/~685.5 mbsf.

Sample	**Mag**	**Mag**	**Mag**	**Mag**	**G**	**G**	**G**	**G**	**P**	**P**	**P**	**P**	**P**	**P**
Figure 4 Part					**a(1)**	**a(2)**	**a(3)**	**b(1)**	**c(1)**	**c(2)**	**c(3)**	**d(1)**	**d(2)**	**d(3)**
SiO_2	n.d.	n.d.	n.d.	n.d.	n.d.	n.d.	n.d.	n.d.	n.d.	n.d.	n.d.	n.d.	n.d.	n.d.
TiO_2	0.0	0.2	0.0	0.1	10.3	11.5	12.4	7.2	1.5	1.3	1.6	1.0	2.0	1.7
Al_2O_3	0.1	0.1	0.1	0.1	0.1	0.1	0.2	0.2	2.0	1.5	1.7	2.4	2.7	1.8
* Fe_2O_3 wt.%	68.3	67.4	68.9	67.2	50.5	47.0	45.2	53.8	61.3	63.2	63.2	65.6	64.2	66.5
* FeO wt.%	30.8	30.5	31.0	30.1	41.3	42.0	42.8	37.0	28.8	29.5	29.8	26.3	25.0	21.9
MnO	n.d.	n.d.	n.d.	n.d.	n.d.	n.d.	n.d.	n.d.	n.d.	n.d.	n.d.	n.d.	n.d.	n.d.
MgO	0.0	0.1	0.0	0.2	0.0	0.0	0.0	0.2	1.6	1.3	1.5	3.7	5.2	6.9
CaO	n.d.	n.d.	n.d.	n.d.	n.d.	n.d.	n.d.	n.d.	n.d.	n.d.	n.d.	n.d.	n.d.	n.d.
Cr_2O_3	n.d.	n.d.	n.d.	n.d.	n.d.	n.d.	n.d.	n.d.	n.d.	n.d.	n.d.	n.d.	n.d.	n.d.
ZnO	n.d.	n.d.	n.d.	n.d.	n.d.	n.d.	n.d.	n.d.	n.d.	n.d.	n.d.	n.d.	n.d.	n.d.
V_2O_3	n.d.	n.d.	n.d.	n.d.	n.d.	n.d.	n.d.	n.d.	n.d.	n.d.	n.d.	n.d.	n.d.	n.d.
NiO	n.d.	n.d.	n.d.	n.d.	n.d.	n.d.	n.d.	n.d.	n.d.	n.d.	n.d.	n.d.	n.d.	n.d.
* Total:	99.1	98.4	100.0	97.6	102.2	100.7	100.6	98.4	95.2	96.8	97.8	99.1	99.0	98.6
* $Fe^{3+}/\sum Fe$	0.69	0.69	0.69	0.69	0.55	0.53	0.51	0.59	0.68	0.68	0.68	0.71	0.72	0.75

Note: FeO and Fe_2O_3 concentrations were calculated using the methods of [40]. Asterisks (*) denote values that are derived from this calculation. The first row contains the sample names (Mag = magnetite standard). The second row indicates which parts within Figure 4 the measurements correspond to (and the specific analyzed grains as numbered in the figure).

Table 2. WDS analyses of additional Fe-oxide grains (oxide wt.%) from samples A/~685.4 mbsf, F/~685.42 mbsf, and G/~685.43 mbsf.

Sample	A	A	F	F	F	F	F	F	F	F	F	G
SiO_2	0.0	0.0	0.0	0.2	0.1	0.1	0.1	0.1	0.0	0.0	0.0	0.1
TiO_2	0.1	0.1	0.2	1.0	0.9	1.0	0.1	0.1	0.1	0.1	0.1	0.2
Al_2O3	0.2	0.2	0.1	1.0	0.7	0.7	0.1	0.0	0.0	0.0	0.1	0.1
* Fe_2O_3 wt.%	66.9	67.3	68.6	66.5	66.9	66.8	68.4	68.6	66.8	68.5	67.4	67.1
* FeO wt.%	29.0	29.3	28.5	27.6	27.4	27.5	30.5	30.6	29.4	30.4	29.8	27.8
MnO	0.1	0.1	0.1	0.3	0.3	0.2	0.1	0.1	0.1	0.1	0.1	0.2
MgO	0.9	0.7	1.5	2.7	2.6	2.7	0.3	0.3	0.5	0.4	0.5	1.5
CaO	0.0	0.0	0.1	0.1	0.1	0.1	0.0	0.0	0.1	0.1	0.1	0.2
Cr_2O_3	0.0	0.0	0.0	0.0	0.0	0.0	0.0	0.0	0.0	0.0	0.0	0.0
V_2O_3	0.3	0.2	0.1	0.0	0.1	0.2	0.2	0.1	0.2	0.2	0.2	0.2
NiO	0.0	0.0	0.0	0.1	0.1	0.0	0.0	0.0	0.0	0.0	0.0	0.0
* Total:	97.4	97.8	99.1	99.2	99.2	99.3	99.8	100.0	97.3	99.7	98.2	97.3
* $Fe^{3+}/\sum Fe$	0.67	0.67	0.68	0.68	0.69	0.69	0.67	0.67	0.67	0.67	0.67	0.68

Note: FeO and Fe_2O_3 concentrations were calculated using the methods of [39]. Asterisks (*) denote values that are derived from this calculation.

The large primary Fe-oxide grains are also associated with smaller (sub-micrometer to micrometer in diameter) Fe-oxide phases along the crystal boundaries (Figure 5a–c). It is unclear whether the decomposition is due to shock metamorphism, entrainment into superheated impact melt, or hydrothermal decomposition. Smaller Fe-oxide minerals (<5 μm) are also visibly dispersed throughout or clustered within partially crystallized impact melt (Figure 5d–f). Many of these grains were too small for mineralogy to be determined using quantitative EDS or WDS. Such Fe-oxide grains may either be secondary minerals precipitated from hydrothermal fluid circulation or primary material. We are unable to conclusively state their origin based on petrographic imaging alone. However, we note that Ti was not detected in EDS measurements of these grains and that Ti concentrations have been observed to be lower in hydrothermal magnetite compared to igneous magnetite [41]. Because Ti is inferred to be relatively immobile in hydrothermal settings [42,43], it may not be readily incorporated into hydrothermally precipitated magnetite. Based on the Curie temperatures produced from susceptibility vs. temperature (k-T) curves from previous rock magnetic studies, stoichiometric magnetite, Ti-bearing magnetite, and maghemite are present within suevite samples, while hematite is not reported [1,44]. This can be useful for deciphering the origin of Fe-oxide phases.

For example, the primary Fe-oxide minerals often contain Ti. In contrast, sub-micrometer to micrometer Fe-oxide minerals concentrated within clay (e.g., smectite group minerals) do not contain Ti and therefore may be hydrothermal in origin (Figure 6). In general, putative hydrothermal Fe-oxide minerals are difficult to locate. EDS and WDS analyses of Fe-oxide crystals smaller than the beam–specimen interaction volume are challenging. Nonetheless, the crystals analyzed contain mostly Fe and O (Figure 6d). Additional elements (such as Si and Al) are incorporated from overlapping and neighboring phases (visible in spectral analyses). The sub-micrometer Fe-oxide crystals in Figure 6 are visible within the smectite clay and have not been seen in the bulk material or in the minerals surrounding them. Hence, we suggest these Fe-oxide minerals may have formed hydrothermally.

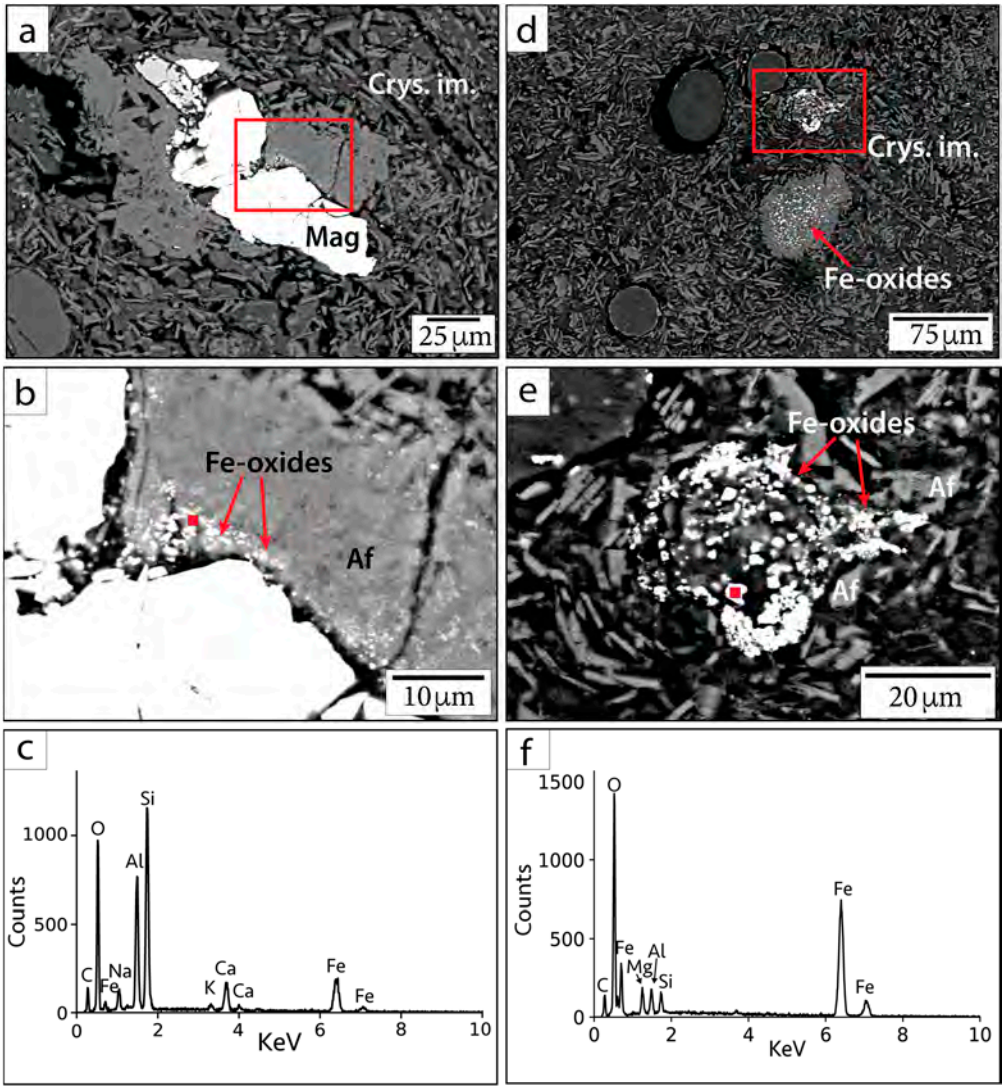

Figure 5. BSE images and EDS spectra of small Fe-oxide crystals in sample 082-2-025/708.7 mbsf. (**a**,**d**) Context BSE images of Fe-oxide occurrences. (**b**,**e**) Magnified image of smaller phases within the red outlined squares in parts (**a**,**d**). (**c**,**f**) EDS spectra corresponding to red points in parts (**b**,**e**). Mag = magnetite, Af = alkali feldspar group minerals, Crys. im. = crystallized impact melt.

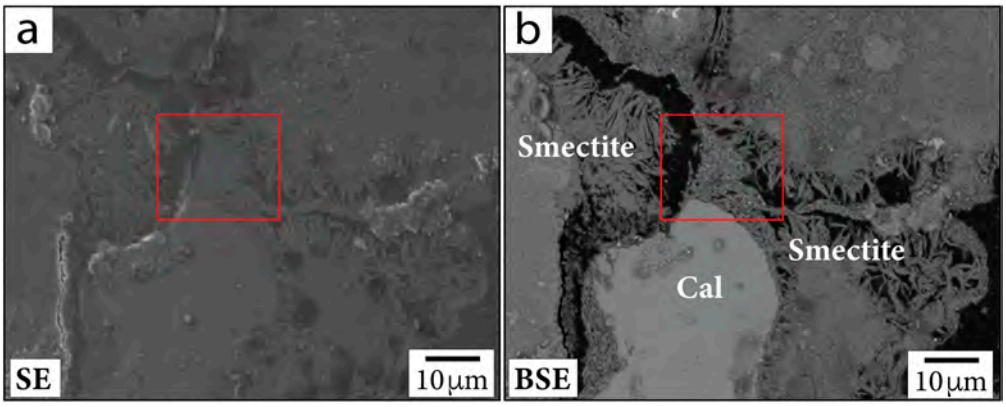

Figure 6. *Cont.*

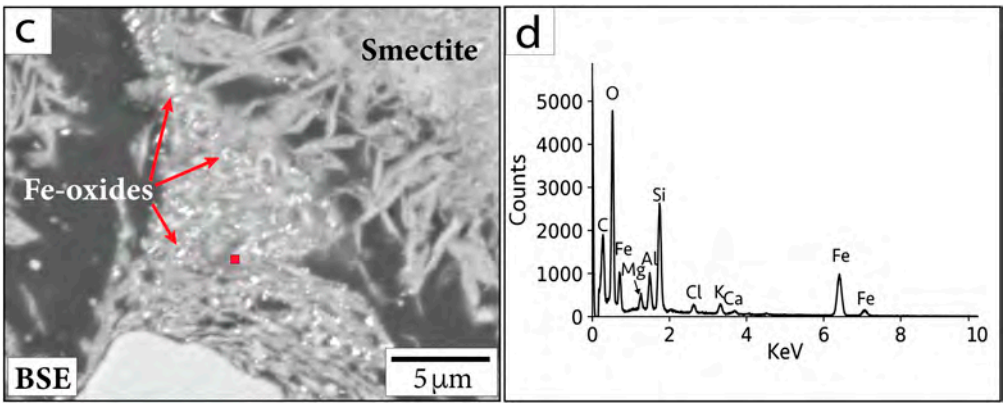

Figure 6. (**a**) SE and (**b**) BSE images of region containing sub-micrometer Fe-oxide crystals in sample P/~685.5 mbsf. (**c**) Magnified image of the area within the red outlined boxes in (**a**,**b**). Red square in (**c**) shows location corresponding to EDS spectrum in (**d**). Cal = calcite. Smectite = smectite group minerals.

3.2. Occurrences of Fe-Sulfide Grains

Various Fe-sulfide minerals occur within the Chicxulub upper peak ring suevite. WDS analyses indicate these sulfides include FeS_2 (pyrite or marcasite), $CuFeS_2$ (chalcopyrite), and Fe,Ni,Co-sulfides (or aggregates of pyrite with Ni-, Cu-, or Co-rich phases) (Figure 7, Table 3). Large (>10 µm diameter), likely primary grains of composition FeS_2 and $CuFeS_2$ are observed within partially crystallized impact melt (Figure 7a,b). Pyrite framboids ~5–30 µm in diameter are also visible within samples near calcite and dachiardite-Na (Figure 7c); these have been well documented by Kring et al. [45].

Table 3. WDS analyses of Fe-sulfide grains (wt. %) in samples F/~685.42 mbsf and P/~685.5 mbsf.

Sample	P	P	P	P	F	F	P	P	P	P	P	P
Figure 7 Part	**a(1)**	**a(2)**	**b(1)**	**b(2)**	**c(1)**	**c(2)**	**e(1)**	**f(1)**	**f(2)**	**g(1)**	**g(2)**	**g(3)**
Mg	0.03	0.07	0.00	0.01	0.00	0.00	0.00	0.00	0.00	0.02	0.01	0.02
Al	0.05	0.07	0.03	0.05	0.01	0.00	0.01	0.02	0.01	0.01	0.05	0.03
S	53.48	53.51	34.54	34.10	53.19	52.86	49.92	53.62	53.20	52.30	52.01	52.85
Cl	0.04	0.07	0.00	0.05	0.01	0.03	n.a.	0.04	0.05	0.04	0.06	0.06
Ca	0.21	0.16	0.17	0.14	0.68	0.50	0.38	0.21	0.26	0.36	0.24	0.15
Ti	0.02	0.05	0.00	0.00	0.00	0.00	0.28	0.42	0.36	0.32	0.34	0.30
Cr	0.01	0.00	0.01	0.00	0.00	0.01	0.03	0.00	0.01	0.00	0.02	0.00
Mn	0.00	0.01	0.03	0.01	0.02	0.02	0.02	0.00	0.00	0.01	0.00	0.00
Fe	46.23	45.98	30.31	30.23	46.28	46.16	36.98	35.99	36.48	31.59	36.53	37.28
Co	0.01	0.02	0.01	0.02	0.00	0.00	2.95	3.22	3.40	5.73	4.69	3.93
Ni	0.00	0.00	0.00	0.00	0.02	0.17	3.67	3.95	4.46	3.61	4.46	4.34
Cu	0.06	0.05	33.38	33.72	0.06	0.08	2.56	2.20	1.94	5.48	0.60	0.71
Ba	n.a.	n.a.	n.a.	n.a.	n.a.	n.a.	0.19	n.a.	n.a.	n.a.	n.a.	n.a.
Si	n.a.	n.a.	n.a.	n.a.	n.a.	n.a.	0.01	n.a.	n.a.	n.a.	n.a.	n.a.
Total:	100.13	99.99	98.48	98.33	100.28	99.82	97.00	99.66	100.17	99.46	99.02	99.67

Note: Results are corrected for spectral interference (CoKα/FeKβ). n.a. = element not analyzed. The first row contains the sample names. The second row indicates which parts within Figure 7 the measurements correspond to (and the specific analyzed grains as numbered in the figure).

Pyrite grains containing Ni, Cu, and Co or aggregates of pyrite with other Ni-, Cu-, and Co-rich phases were found in sample 081-2-025/708.8 mbsf and sample P/685.5 mbsf (Figure 7d–g). These Fe-sulfide occurrences exhibit a variety of shapes, usually containing aggregates of subrounded grains roughly a few micrometers in diameter, and are seen filling in voids. We note that slightly low totals in WDS data for some analyses (~97–98 wt.%) may be due to grain or aggregate topography, missing elements in the surrounding matrix, void spaces, or epoxy given the small grain sizes measured. The Fe-sulfide crystals within

sample P are located within a large, secondary, $CaCO_3$ mineral grain (sparry calcite) that may have grown due to impact-related heating. These grains are associated with a secondary Ti-rich phase. Anatase, rutile (TiO_2), and titanite ($CaTiSiO_5$) have previously been identified in suevite samples [1]. The presence of Ca in EDS spectra suggests that the phase may be titanite.

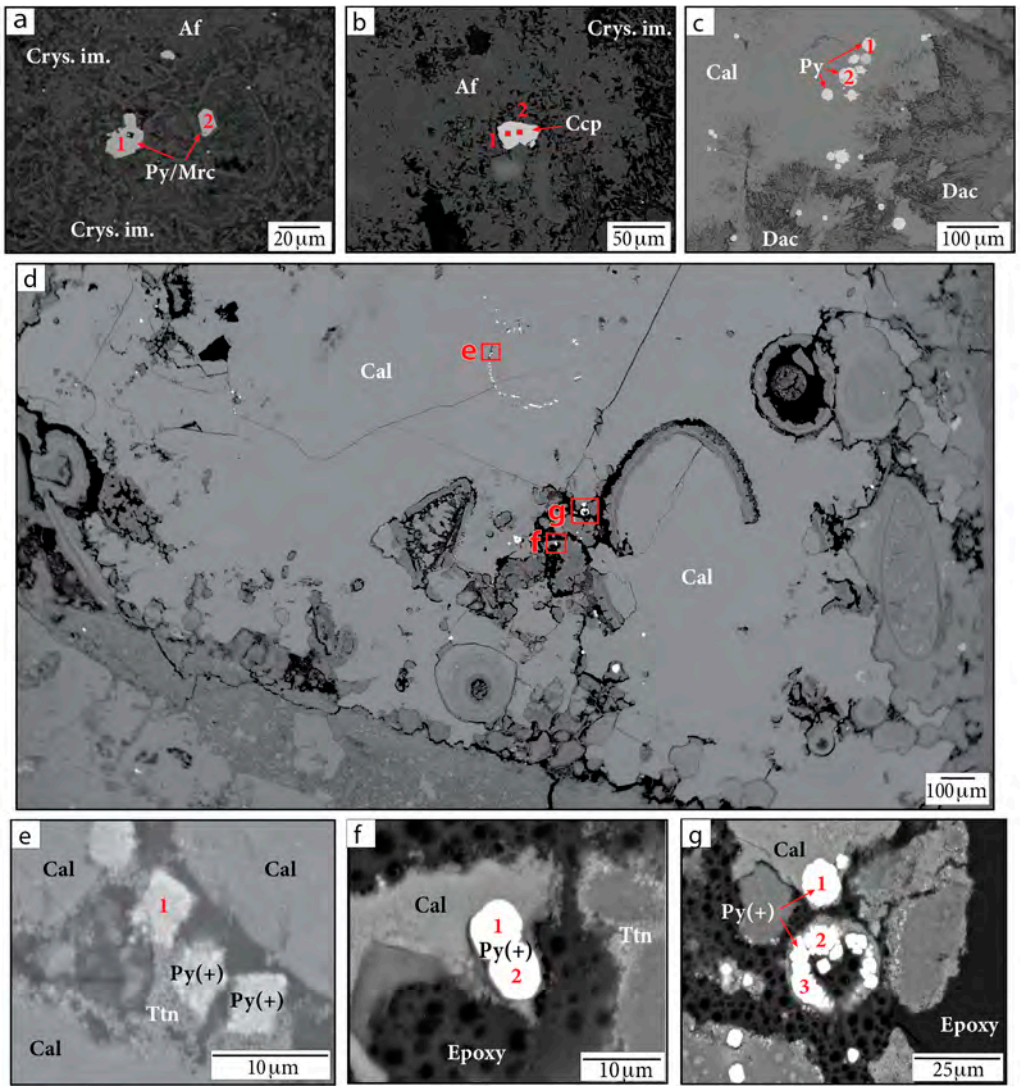

Figure 7. BSE images of Fe-sulfide grains in (**a**,**b**,**d**–**g**) sample P/~685.5 mbsf and in (**c**) sample F/~685.42 mbsf. Figure parts (**e**,**f**) show magnified images of the red outlined regions in part (**d**). Numbers indicate locations of WDS analyses. Af = alkali feldspar group minerals. Cal = calcite. Ccp = chalcopyrite. Crys. im. = crystallized impact melt. Dac = dachiardite-Na. Py/Mrc = pyrite or marcasite. Py(+) = either Ni-, Cu-, or Co-bearing pyrite or aggregates of pyrite crystals with other Ni-, Cu-, and Co-bearing phases. Smectite = smectite group minerals. Ttn = titanite.

Sub-micrometer to micrometer Fe-sulfide phases are also visible within clay (smectite) rims infilling voids and along fractures within crystallized impact melt (Figure 8). WDS analyses of these small grains were generally unsuccessful, precluding robust mineral identifications based on composition. EDS analyses of these small Fe-sulfide crystals are affected by overlapping and neighboring minerals; however, the EDS spectra indicate these grains contain mostly Fe and S (Figure 8).

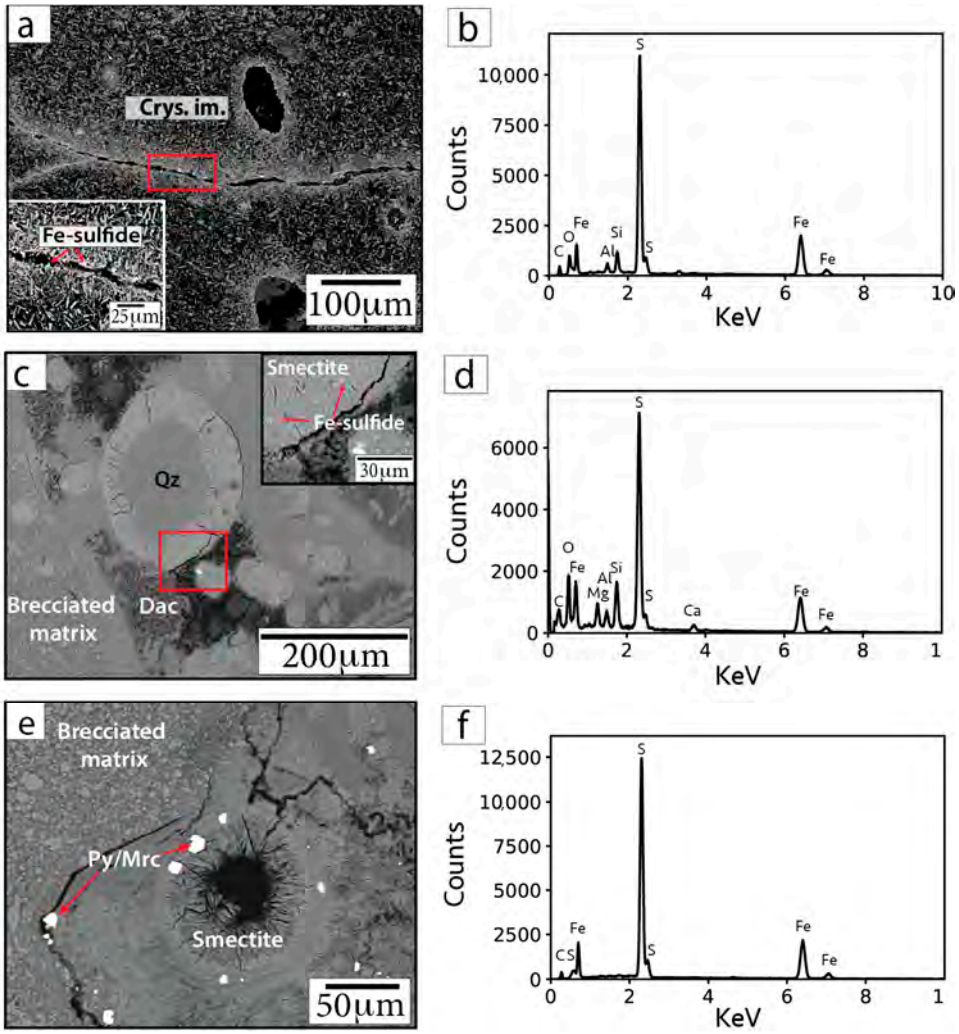

Figure 8. BSE images (**a**,**c**,**e**) and representative EDS spectra (**b**,**d**,**f**) of Fe-sulfide grains in sample F/~685.42 mbsf. Insets in parts (**a**) and (**c**) show magnified images of the areas within the red outlined boxes. Arrows point to locations targeted for EDS analyses. Cal = calcite. Smectite = smectite group minerals.

4. Discussion

4.1. The Occurrence of Fe-Oxide and Fe-Sulfide Minerals, and Clay

While the context of some Fe-oxide and Fe-sulfide minerals can be obvious, such as inherited primary grains, the natures of many phases are elusive. Quantitative X-ray microanalysis (EDS and WDS) is only possible for grains that are larger than the beam–specimen interaction volume, which is dependent on sample composition and analytical conditions. Monte Carlo simulations of electron trajectories in programs such as CASINO [46,47] yield diameters of the interaction volumes on the order of 3 to 5 µm for Fe-Ti oxides and Fe-sulfides at 15 kV. Many of the oxides and sulfides in our samples are within or smaller than this size range, and therefore EDS and WDS analyses often contain X-rays generated by surrounding materials. For larger grains, analytical spots were chosen, where possible, within a homogeneous region and several micrometers away from surface imperfections (pits, cracks), grain boundaries, inclusions, and intergrowths. However, many grains have heterogeneous textures. Therefore, our analyses are considered to represent both the targeted grain and any primary lamellae, inclusions, or intergrowths, and/or secondary replacement textures (e.g., TiO_2 rims and lamellae in Figure 4a). For these reasons, quantitative identification of the oxides and sulfides is not always possible. A recent study of hydrothermal alteration within Hole M0077A reports unresolvable

micrometer-sized oxides within devitrified glass clasts [48]. Our imaging results reveal that sub-micrometer to micrometer Fe-oxide crystals are also associated with clay. We acknowledge that our EDS/WDS results reflect the limitations of the use of SEM/EPMA to quantify such small phases; however, it is evident that the crystals analyzed contain pure Fe-cation spikes and are likely magnetite or maghemite (based on previous rock magnetic property analyses) and that their EDS spectra contain elements from overlapping and surrounding clay minerals. Similar methods have been used to document the growth of authigenic micrometer-scale magnetite crystals in Devonian carbonates [49,50]. Weil et al. [49] report that Fe-oxide minerals were found in association with likely fluid pathways such as cracks, veins, and grain boundaries. The cogenetic relationship between Fe-oxide minerals and fluid pathways implies that the authigenic reaction took place within fluids. Comparably, we interpret the Fe-rich minerals located in cracks, veins, grain boundaries, and clay-infilled voids within our samples to be evidence of precipitated phases due to hydrothermal fluid flow. Subsequent studies would benefit from additional quantitative techniques such as X-ray diffraction, Raman spectroscopy, and the use of fresh, unpolished surfaces to verify our EDS- and WDS-based interpretations.

No pristine impact melt glass is preserved within suevite subunit 2B as it has been replaced by Fe-Mg-rich smectite [29,30]. Simpson et al. [48] documented that both fine- and coarse-grained smectite clays derived from impact glasses are often associated with Fe-Ti oxide minerals as well as a cryptocrystalline, hydrated, smectite-like phase. The occurrence of impact glass fragments that have been altered to Fe-rich smectite may be associated with the formation of authigenic magnetite seen in our samples. The formation of such a phase involves the remobilization of all elements involved in the alteration process, forming elemental depletions or enrichments. This process is likely dependent on temperature, the structures of primary and secondary phases, and fluid properties, such as pH and oxygen fugacity [51]. Oxygen and hydrogen isotope compositions of the smectitic clay minerals hinted that smectite clays within Chicxulub upper peak ring suevite samples may have formed at temperatures of ~20–50 °C [48]. However, current ambient conditions for the suevite interval (619–756 mbsf) buried beneath 617 m of post-impact sedimentary rocks are 49–54 °C [31]. Simpson et al. [48] proposed that smectites may have formed below current ambient temperatures due to the alteration of suevite before the overlying sedimentary rocks were deposited. Alternatively, the paleotemperature inferred in [48] may represent the temperature at which the clay fraction equilibrated with fluid at the end of the reaction sequence.

4.2. Rock Magnetic Implications

It is unclear how hydrothermal precipitation at temperatures <150 °C may affect the magnetic recording properties of secondary Fe-oxide minerals. If hydrothermally precipitated magnetic minerals form in the presence of an ambient magnetic field, they will record CRM. Pilkington et al. [52] report on secondary magnetite formed from hydrothermal alteration at temperatures <150 °C in Chicxulub drill core Yaxcopoil-1. They describe the secondary phase as vesicle infillings associated with clay minerals and as fine aggregates between plagioclase/diopside laths in the melt rock. Suevite samples that contain these phases in Yaxcopoil-1 are generally paramagnetic (bulk sample) and have weak natural remanent magnetizations (~0.1 A/m) compared to the natural remanent magnetization of a sample that contains an inherited mafic basement clast (77.5 A/m). Thermoremanent magnetization (TRM) that is stable over geologic time is most efficiently acquired by magnetite in the stable single domain or pseudosingle domain size range, ~0.05 to ~1 µm (though the critical domain state size boundaries may vary based on shape and composition) [53,54]. Our results from Hole M0077A show Fe-oxide crystals with diameters of ~0.5 µm, capable of recording high-fidelity magnetic remanences as demonstrated by Kring et al. [1]. In addition to hydrothermally precipitated sub-micrometer Fe-oxide minerals, our imaging results reveal the alteration of primary Ti-bearing magnetite grains via thermal or hydrothermal decomposition within fractures and pits, as well as along the edges of grains (Figure 4a,b),

which likely led to the formation of smaller grains (Figure 4d). Impurities such as Al, Mg, Si, and Mn may also be attributable to dissolution [55]. Such patterns demonstrate how rocks may become overprinted with magnetic remanences such as TRM due to impact heating or CRM from post-impact hydrothermal alteration. Previous work has shown that primary TRMs within rocks that are modified by low-temperature chemical processes, such as grain dissolution and oxidation, can produce incorrect estimations of geomagnetic paleointensities [56,57]. After an initial remanence is acquired, further oxidation of magnetite may produce CRMs that could record changes in the geomagnetic field over time [58]. Future work should focus on exploring the magnetic parameters of minerals such as magnetite, maghemite, and hematite that are produced by hydrothermal precipitation or dissolution to understand how these contribute to bulk remanent magnetization and associated magnetic anomalies produced during protracted cooling within impact structures.

4.3. Moderately Siderophile Elements

Our detailed examination of sample P/~685.5 mbsf shows that Ni and Co can be hydrothermally leached from target lithologies or potentially impactor-sourced materials and incorporated within secondary Fe-sulfide phases. These phases occur in fractures and voids, outlining their origin as hydrothermally precipitated secondary phases. However, the aforementioned siderophile elements occur as trace elements and are not observed in most secondary Fe-sulfide phases seen throughout our suevite samples. In fact, only two out of eight samples analyzed for this study contain Fe-sulfide minerals that incorporated the moderately siderophile elements Ni and Co. Moreover, within sample P, all the Ni- and Co-containing grains were located within ~100–400 μm from each other, suggesting that localized solution-precipitation conditions triggered their crystallization during hydrothermal alteration.

Within the melt sheets of the Sudbury impact structure, the separation of sulfides containing Ni-Cu-PGEs occurred at ~1400 °C when sulfide saturation was achieved [59]. The sulfide melt is stratified to the lower melt sheet during differentiation [23,60]. While impact melts can reach temperatures >2370 °C initially [61], the temperature of the melt sheet may be significantly lowered due to the assimilation of clasts within the melt [62]. An initial temperature of 1700 °C for the impact melt sheet at Chicxulub has been used in modeling to calculate the duration of post-impact hydrothermal activity [63]. Previously sampled impact melt rocks from Chicxulub were found to be fine-grained and andesitic in composition, showing little evidence of fractional crystallization compared to those from the Sudbury impact melt sheet. It is possible the enhanced differentiation in the Sudbury melt rocks is due to previous warming from orogenic activity in the Sudbury region [64]. Chicxulub melt rocks sampled thus far were sourced from relatively shallow depths. Therefore, it is unclear whether the Chicxulub melt sheet underwent significant differentiation. Future sampling through the entirety of the melt sheet at Chicxulub may provide resolution. However, seismic and aeromagnetic data may suggest that the crater floor of Chicxulub may contain exhalative sulfide deposits, similar to those found on the Sudbury crater floor [65]. Within the transitional zone of Hole M0077A, between the suevite of the upper peak ring and the post-impact carbonate sedimentary rocks (616.58–617.33 mbsf), rounded pyrite grains zoned with a center of up to 3% Ni were reported [66]. These sulfide phases may be the products of high-temperature, early hydrothermal venting within the crater [66] and reflect hydrothermal redistribution of deeper crustal components or meteoritic components [67]. The ~5 μm diameter Ni-bearing pyrite grains seen in sample P are compositionally and morphologically similar to the ~40 μm diameter grains reported in [66], raising the possibility that they may have been formed by similar high-temperature venting processes despite their differing sizes. Increased manganese abundances are reported in the transitional unit and the overlying carbonate sedimentary rocks [1]. Based on micropaleontology of the sedimentary rocks, this would imply that hydrothermal venting continued for at least ~2.1 million years [1].

4.4. Astrobiological Perspectives

Crystalline minerals are linked to the origin of life, acting as templates and catalyzers for the first biomolecules [68] and in protecting pre-biotic molecules (i.e., amino acids, organics) in the space environment [69]. Clay minerals, formed from the aqueous alteration of silicate minerals, may have played an instrumental role in the initiation of the evolution of life on Earth and in shielding it from ultraviolet radiation [70]. Clays such as smectite act as catalysts for precursory organic molecules and contain charged surfaces that are able to adsorb organic compounds, facilitating replication [71–74]. Smectite, water, and organic molecules can collectively generate conditions for the formation of more complex organic molecules [71]. Specifically, Fe-rich smectites have high catalytic potential and may have acted as microenvironments during early hydrothermal activity in the Hadean [75]. Hydrothermal microenvironments such as these may have facilitated the origin of life during a hostile time in Earth's past, when large impacts occurred more frequently [76]. Our investigation of the hydrothermally altered suevite from the Chicxulub impact structure may also be a terrestrial analog for the processes and resulting microenvironments that may have occurred on other rocky planets in the solar system which contained water in their crust. Moreover, organic matter associated with clay minerals in carbonaceous chondrites may demonstrate the ability of clay to promote the polymerization of organic pre-biotic molecules even before the origin of life on Earth [77]. Therefore, areas that contain Fe-rich smectite and conditions where Fe-oxide phases can donate electrons could be of astrobiological interest.

Fe-sulfide minerals are also biologically interesting. The formation of pyrite from hydrogen sulfide and ferrous ions may have been an energy source for the origin of life [78]. In early Earth hydrothermal settings, it is thought that sulfides may have supplied energy and catalyzed reactions, leading to complex organic molecules [79]. Some secondary pyrite grains seen in our samples appear to have colloidal structures (Figure 7) and may represent the diagenesis of pyrite framboids due to overgrowth, recrystallization, or cementation as inferred for similar grains in [80]. Kring and Bach [38] report on pyrite framboids with isotopic compositions that reflect microbial sulfate-reduction near altered glass fragments within Chicxulub suevite samples. The alteration of glass fragments may have produced sufficient amounts of hydrogen to fuel a subsurface microbial community of thermophiles and hyperthermophiles which thrived in permeable niches of the suevite within the crater [38]. Similarly, if life were present on a planet such as Mars that experienced hydrothermal activity in its past, then it too could have utilized sulfate reduction as an energy source. For such reasons, documenting the collective qualities and spatial relationships of Fe- and S-rich minerals in hydrothermally altered impact rocks is useful for ongoing astrobiology research which aims to identify a precursory setting for life to emerge and evolve.

5. Conclusions

Our petrographic examination of suevite samples from the Chicxulub crater peak ring documents the occurrence of Fe-oxide and Fe-sulfide minerals (including magnetite; Ti-bearing magnetite; maghemite; pyrite or marcasite; chalcopyrite; and Ni-, Cu-, and Co-bearing sulfide phases). Large (~10–100 μm) primary Fe-oxide and Fe-sulfide minerals occur, some displaying evidence of impact deformation and, in some cases, decomposition or dissolution attributable to impact heating or hydrothermal alteration, respectively. Smaller (sub-micrometer to micrometer) Fe-oxide and Fe-sulfide phases are easily identifiable in BSE imaging and EDS analyses; however, interpreting their origin can be complex. We therefore rely on the petrographic context and surrounding mineral phases to determine truly secondary phases so that we may explore the hydrothermal fluid-driven migration of Fe and siderophile elements within the suevite. We observed sub-micrometer Fe-oxide crystals within clay. These Fe-oxide minerals presented are not seen in surrounding or neighboring mineral phases. The nature of the very small grains makes quantifying their elemental abundances difficult. The formation of Fe-oxide minerals within smectite demon-

strates how secondary crystalline minerals may contribute to microenvironments that favor the development of complex organic molecules. Fe-sulfide minerals are visible throughout the samples. It is common to see micrometer- to sub-micrometer-sized crystals specifically within rims around clasts, clay, and vesicles; within clay; and lining fractures crosscutting crystallized impact melt. Cu is present in Fe-sulfide minerals (chalcopyrite) in a variety of occurrences (e.g., rims, matrix, smectite). The incorporation of Ni and Co into sulfide phases is rarer. The presence of Ni-, Cu-, and Co-rich Fe-sulfide grains demonstrates how siderophile elements may be remobilized from target lithologies or impactor-derived materials and incorporated into hydrothermally altered suevite. Additionally, secondary Fe-sulfide minerals may represent the availability of microbial energy sources such as sulfate reduction. The continued characterization of Fe-oxide and Fe-sulfide minerals within impact crater rocks will elucidate evolving chemical conditions of the Chicxulub hydrothermal system, providing experimental constraints on post-impact cratering processes and the associated development of microenvironments that could benefit life.

Author Contributions: Conceptualization, C.M.V. and S.M.T.; methodology, C.M.V., S.M.T., L.W., J.-I.J. and D.H.B.; formal analysis, C.M.V. and J.-I.J.; resources, S.M.T., S.B., L.W. and D.H.B.; data curation, S.M.T.; writing—original draft preparation, C.M.V. and S.M.T.; writing—review and editing, J.-I.J., A.W., D.A.K., S.B., L.W. and S.P.S.G.; project administration, S.M.T.; funding acquisition, S.M.T., D.A.K. and S.P.S.G. All authors have read and agreed to the published version of the manuscript.

Funding: This research was funded by the U.S. National Aeronautics and Space Administration (NASA), grant number 80NSSC20K1528, as well as institutional support from Rutgers University and Stanford University. C.M.V. was also supported by a U.S. National Science Foundation graduate fellowship, grant number 1842213.

Data Availability Statement: SEM/EDS and EPMA/WDS images and data from this study are available on Zenodo, a permanent CERN-backed online data repository, at DOI:10.5281/zenodo.7674024. Interested investigators may request samples or data from Expedition 364 by placing an IODP Sample and Data Request at http://web.iodp.tamu.edu/sdrm/ (accessed 23 February 2023).

Acknowledgments: We thank E. Karadeema (High Mesa Petrographics) for thin section preparation and helpful discussions. This is University of Texas Institute for Geophysics Contribution #3953, University of Texas Center for Planetary Systems Habitability (CPSH) Contribution #0062, and LPI Contribution #2879. LPI is operated by USRA under a cooperative agreement with the Science Mission Directorate of the National Aeronautics and Space Administration.

Conflicts of Interest: The authors declare no conflict of interest. The funders had no role in the design of the study; in the collection, analyses, or interpretation of data; in the writing of the manuscript; or in the decision to publish the results.

References

1. Kring, D.A.; Tikoo, S.M.; Schmieder, M.; Riller, U.; Rebolledo-Vieyra, M.; Simpson, S.L.; Osinski, G.R.; Gattacceca, J.; Wittmann, A.; Verhagen, C.M.; et al. Probing the hydrothermal system of the Chicxulub crater. *Sci. Adv.* **2020**, *6*, eaaz3053. [CrossRef]
2. Kring, D.A.; Boynton, W.V. The petrogenesis of an augite-bearing melt rock in the Chicxulub structure and its relationship to K/T impact spherules in Haiti. *Nature* **1992**, *358*, 141–144. [CrossRef]
3. McCarville, P.; Crossey, L.J. Post-impact hydrothermal alteration of the Manson impact structure. In *The Manson Impact Structure, Iowa*; Special Paper 302; Koeberl, C., Anderson, R., Eds.; Geological Society of America: Boulder, CO, USA, 1996; pp. 347–376.
4. Boer, R.; Reimold, W.U.; Koeberl, C.; Kessler, S.E. Fluid inclusion studies on drill core samples from the Manson impact crater, Iowa: Evidence for post-impact hydrothermal activity. In *The Manson Impact Structure, Iowa*; Special Paper 302; Koeberl, C., Anderson, R., Eds.; Geological Society of America: Boulder, CO, USA, 1996; pp. 377–382.
5. Naumov, M.V. Zeolite mineralization in impact craters. *Zap. Vsesoyuznogo Mineral. Obs.* **1993**, *122*, 1–2. (In Russian)
6. Naumov, M.V. Basic regularities of the postimpact hydrothermal process. *Sol. Syst. Res.* **1996**, *30*, 21–27.
7. Naumov, M.V. Hydrothermal-mesosomatic mineralization. In *Deep Drilling in the Puchezh-Katunki Impact Structure*; Masaitis, V., Pevzner, L., Eds.; VSEGEL: St. Petersburg, Russia, 1999; pp. 276–286. (In Russian)
8. Jelen, B.I.; Giovannelli, D.; Falkowski, P.G. The role of microbial electron transfer in the coevolution of the biosphere and geosphere. *Annu. Rev. Microbiol.* **2016**, *70*, 45–62. [CrossRef] [PubMed]

9. Bryce, C.; Blackwell, N.; Schmidt, C.; Otte, J.; Huang, Y.-M.; Kleindienst, S.; Tomaszewski, E.; Schad, M.; Warter, V.; Peng, C.; et al. Microbial anaerobic Fe(II) oxidation—Ecology, mechanisms and environmental implications. *Environ. Microbiol.* **2018**, *20*, 3462–3483. [CrossRef]
10. Cockell, C.S.; Schaefer, B.; Wuchter, C.; Coolen, M.J.L.; Grice, K.; Schnieders, L.; Morgan, J.V.; Gulick, S.P.S.; Wittmann, A.; Lofi, J.; et al. Shaping of the present-day deep biosphere at Chicxulub by the impact catastrophe that ended the Cretaceous. *Front. Microbiol.* **2021**, *12*, 668240. [CrossRef]
11. Cockell, C.S.; Lee, P. The biology of impact craters—A review. *Biol. Rev.* **2002**, *77*, 279–310. [CrossRef]
12. Kring, D.A. Impact events and their affect on the origin, evolution, and distribution of life. *GSA Today* **2000**, *10*, 1–7.
13. Osinski, G.R.; Tornabene, L.L.; Banerjee, N.R.; Cockell, C.S.; Flemming, R.; Izawa, M.R.M.; McCutcheon, J.; Parnell, J.; Preston, L.J.; Pickersgill, A.E.; et al. Impact-generated hydrothermal systems on Earth and Mars. *Icarus* **2013**, *224*, 347–363. [CrossRef]
14. Koeberl, C.; Reimold, W.U. Post-impact hydrothermal activity in meteorite impact craters and potential opportunitites for life. In *Bioastronomy 2002: Life among the Stars*; (IAU Symposium 213); Norris, R., Stootman, F., Eds.; Astronomical Society of the Pacific: San Francisco, CA, USA, 2004; pp. 299–304.
15. Epstein, J.; Pittarello, L.; Crósta, A.P.; Koeberl, C. Impact-induced hydrothermal dissolution in pyroxene: Petrographic and geochemical characterization of basalt-dominated polymict impact breccias from the Vargeão Dome, Brazil. In *Large Meteorite Impacts and Planetary Evolution IV*; Special Paper 550; Reimold, W., Koeberl, C., Eds.; Geological Society of America: Boulder, CO, USA, 2021; pp. 537–549.
16. Butler, R.F. *Paleomagnetism: Magnetic Domains to Geologic Terranes*; Blackwell: Oxford, UK, 1992.
17. Urrutia-Fucugauchi, J.; Soler-Arechalde, A.M.; Rebolledo-Vieyra, M.; Vera-Sanchez, P. Paleomagnetic and rock magnetic study of the Yaxcopoil-1 impact breccia sequence, Chicxulub impact crater (Mexico). *Meteorit. Planet. Sci.* **2004**, *39*, 843–856. [CrossRef]
18. Velasco-Villareal, M.; Urrutia-Fucugauchi, J.; Rebolledo-Vieyra, M.; Perez-Cruz, L. Paleomagnetism of impact breccias from the Chicxulub crater—Implications for ejecta emplacement and hydrothermal processes. *Phys. Earth Planet. Inter.* **2011**, *186*, 154–171. [CrossRef]
19. Kuzina, D.M.; Gattacceca, J.; Bezaeva, N.S.; Badyukov, D.D.; Rochette, P.; Quesnel, Y.; Demory, F.; Borschneck, D. Paleomagnetic study of impactites from the Karla impact structure suggests protracted postimpact hydrothermalism. *Meteorit. Planet. Sci.* **2022**, *57*, 1846–1860. [CrossRef]
20. Alvarez, L.W.; Alvarez, W.; Asaro, F.; Michel, H.V. Extraterrestrial cause for the Cretaceous-Tertiary extinction. *Science* **1980**, *208*, 1095–1108. [CrossRef] [PubMed]
21. Trinquier, A.; Birck, J.-L.; Allègre, C.J. The nature of the KT impactor. A ^{54}Cr reappraisal. *Earth Planet. Sci. Lett.* **2006**, *241*, 780–788. [CrossRef]
22. Keays, R.; Lightfoot, P. Formation of Ni-Cu platinum group element sulfide mineralization in the Sudbury impact melt sheet. *Miner. Petrol.* **2004**, *82*, 217–258. [CrossRef]
23. Huber, M.S.; Kovaleva, E.; Wilke, F. First Observation of Ni-Cu-Au-PGE Mineralization within Impact Melt of the Vredefort Structure. ICF-CIRIR Abstract. 2022. Available online: https://cirir-edu.org/wp-content/uploads/2022/05/ICF-CIRIR-2022-S2T8-Huber-et-al.pdf, (accessed on 17 February 2023).
24. Hildebrand, A.R.; Penfield, G.T.; Kring, D.A.; Pilkington, M.; Camargo, Z.; Jacobsen, A.; Stein, B.; Boynton, W.V. Chicxulub Crater: A possible Cretaceous/Tertiary boundary impact crater on the Yucatán Peninsula, Mexico. *Geology* **1991**, *19*, 867–871. [CrossRef]
25. Morgan, J.V.; Gulick, S.P.S.; Bralower, T.J.; Chenot, E.; Christeson, G.L.; Claeys, P.; Cockell, C.; Collins, G.S.; Coolen, M.J.L.; Ferrière, L.; et al. The formation of peak rings in large impact craters. *Science* **2016**, *354*, 878–882. [CrossRef] [PubMed]
26. Christeson, G.L.; Gulick, S.P.S.; Morgan, J.V.; Gebhardt, C.; Kring, D.A.; Le Ber, E.; Lofi, J.; Nixon, C.; Poelchau, M.; Rae, A.S.P.; et al. Extraordinary rocks from the peak ring of the Chicxulub impact crater: P-wave velocity, density, and porosity measurements from IODP/ICDP Expedition 364. *Earth Planet. Sci. Lett.* **2018**, *495*, 1–11. [CrossRef]
27. Tagle, R.; Erzinger, J.; Hecht, L.; Schmitt, R.T.; Stöffler, D.; Claeys, P. Platinum group elements in the impactites of the IDCP Chicxulub drill core Yaxcopoil-1: Are there traces of the projectile? *Meteorit. Planet. Sci.* **2010**, *39*, 1009–1016. [CrossRef]
28. Gelinas, A.; Kring, D.A.; Zurcher, L.; Urrutia-Fucugauchi, J.; Morton, O.; Walker, R.J. Osmium isotope constraints on the proportion of bolide component in Chicxulub impact melt rocks. *Meteorit. Planet. Sci.* **2004**, *39*, 1003–1008. [CrossRef]
29. Morgan, J.; Gulick, S.; Mellett, C.L.; Green, S.L. *Expedition 364 Scientists. Chicxulub: Drilling the K-Pg Impact Crater*; International Ocean Discovery Program, 364; International Ocean Discovery Program: College Station, TX, USA, 2017.
30. Simpson, S.L.; Osinski, G.R.; Longstaffe, F.J.; Schmieder, M.; Kring, D.A. Hydrothermal alteration associated with the Chicxulub impact crater upper peak-ring breccias. *Earth Planet. Sci. Lett.* **2020**, *547*, 116425. [CrossRef]
31. Feignon, J.-G.; Schulz, T.; Ferrière, L.; Goderis, S.; de Graaff, S.J.; Kaskes, P.; Déhais, T.; Claeys, P.; Koeberl, C. Search for a meteoritic component within the impact melt rocks of the Chicxulub impact structure peak rink, Mexico. *Geochim. Cosmochim. Acta* **2022**, *323*, 74–101. [CrossRef]
32. Gulick, S.; Morgan, J.; Mellett, C.L.; Green, S.L.; Bralower, T.; Chenot, E.; Christeson, G.; Claeys, P.; Cockell, C.; Coolen, M.J.L.; et al. Site M0077: Upper Peak Ring. In *Chicxulub: Drilling the K-Pg Impact Crater*; Morgan, J., Gulick, S., Mellett, C.L., Green, S.L., Scientists, E., Eds.; International Ocean Discovery Program: College Station, TX, USA, 2017; Volume 364, pp. 1–23.
33. Kaskes, P.; de Graaff, S.J.; Feignon, J.-G.; Déhais, T.; Goderis, S.; Ferrière, L.; Koeberl, C.; Smit, J.; Wittmann, A.; Gulick, S.P.S.; et al. Formation of the crater suevite sequence from the Chicxulub peak ring: A petrographic, geochemical, and sedimentological characterization. *Geol. Soc. Am. Bull.* **2021**, *134*, 895–927. [CrossRef]

34. Gulick, S.P.S.; Bralower, T.J.; Ormo, J.; Hall, B.; Grice, K.; Schaefer, B.; Lyons, S.; Freeman, K.H.; Morgan, J.V.; Artemieva, N.; et al. The first day of the Cenozoic. *Proc. Natl. Acad. Sci. USA* **2019**, *116*, 19342–19351. [CrossRef]
35. Osinski, G.R.; Grieve, R.A.F.; Hill, P.J.A.; Simpson, S.L.; Cockell, C.; Christeson, G.L.; Ebert, M.; Gulick, S.; Melosh, H.J.; Riller, U.; et al. Explosive interaction of impact melt and seawater following the Chicxulub impact event. *Geology* **2020**, *48*, 108–112. [CrossRef]
36. Kring, D.A. The dimensions of the Chicxulub impact crater and impact melt sheet. *J. Geophys. Res.* **1995**, *100*, 16979–16986. [CrossRef]
37. Schulte, F.M.; Wittmann, A.; Jung, S.; Morgan, J.V.; Gulick, S.P.S.; Kring, D.A.; Grieve, R.A.F.; Osinski, G.R.; Riller, U. IODP-ICDP Expedition 364 Science Party. Ocean resurge-induced impact melt dynamics on the peak-ring of the Chicxulub impact structure, Mexico. *Int. J. Earth Sci.* **2021**, *110*, 2619–2636. [CrossRef]
38. Kring, D.A.; Bach, W. Hydrogen production from alteration of Chicxulub Crater impact breccias: Potential energy source for a subsurface microbial ecosystem. *Astrobiology* **2021**, *21*, 1547–1564. [CrossRef]
39. Heinrich, K.F.J. Strategies of electron microprobe data reduction. In *Electron Probe Quantification*; Heinrich, K.F.J., Newbury, D.E., Eds.; Springer Science: New York, NY, USA, 1997; pp. 9–18.
40. Carmichael, I.S.E. The iron-titanium oxides of salic volcanic rocks and their associated ferromagnesian silicates. *Contr. Mineral. and Petrol.* **1967**, *14*, 36–64. [CrossRef]
41. Nadoll, P.; Angerer, T.; Mauk, J.L.; French, D.; Walshe, J. The chemistry of hydrothermal magnetite: A review. *Ore Geol. Rev.* **2014**, *61*, 1–32. [CrossRef]
42. Mathieu, L. Quantifying hydrothermal alteration: A review of methods. *Geosciences* **2018**, *8*, 245. [CrossRef]
43. Petersen, M.D. The use of the "immobile" elements Zr and Ti in lithogeochemical exploration for massive sulphide deposits in the Precambrian Pecos Greenstone Belt of northern New Mexico. *J. Geochem. Explor.* **1983**, *19*, 615–617. [CrossRef]
44. Fucugauchi, J.U.; Perez-Cruz, L.L.; Rebolledo-Vieyra, M.; Tikoo, S.; Zylberman, W.; Lofi, J. Rock magnetic study of IODP/ICDP Expedition 364 Site M0077A drill cores: Post-impact sediments, impact breccias, melt, granitic basement and dikes. In Proceedings of the American Geophysical Union, Fall Meeting 2017, abstract #P33D-2903, New Orleans, LA, USA, 11–15 December 2017.
45. Kring, D.A.; Whitehouse, M.J.; Schmieder, M. Microbial sulfur isotope fractionation in the Chicxulub hydrothermal system. *Astrobiology* **2021**, *21*, 103–114. [CrossRef]
46. Hovington, P.; Drouin, D.; Gauvin, R. CASINO: A new monte carlo code in C language for electron beam interaction-part 1: Description of the program. *Scanning* **1997**, *19*, 1–14. [CrossRef]
47. Drouin, D.; Couture, A.R.; Joly, D.; Tastet, X.; Aimez, V. CASINO V2.42—A fast and east-to-use modeling tool for scanning electron microscopy and microanalysis users. *Scanning* **2007**, *29*, 92–101. [CrossRef]
48. Simpson, S.L.; Longstaffe, F.J.; Osinski, G.R.; Caudill, C.M.; Kring, D.A. A low-temperature, meteoric water-dominated origin for smectitic clay minerals in the Chicxulub impact crater upper peak ring, as inferred from their oxygen and hydrogen isotope compositions. *Chem. Geol.* **2022**, *588*, 120639. [CrossRef]
49. Weil, A.B.; Van der Voo, R. Insights into the mechanism for orogen-related carbonate remagnetization from growth of authigenic Fe-oxide: A scanning electron microscopy and rock magnetic study of Devonian carbonates from northern Spain. *J. Geophys. Res.* **2002**, *107*, EPM-1. [CrossRef]
50. Suk, D.; Van der Voo, R.; Peacor, D.R. Origin of magnetite responsible for remagnetization of early Paleozoic limestones of New York state. *J. Geophys. Res.* **1993**, *98*, 419–434. [CrossRef]
51. Stroncik, N.A.; Schmincke, H.-U. Palagonite—A review. *Int. J. Earth Sci.* **2002**, *91*, 680–697. [CrossRef]
52. Pilkington, P.; Ames, D.E.; Hildebrand, A.R. Magnetic mineralogy of the Yaxcopoil-1 core, Chicxulub. *Meteorit. Planet. Sci.* **2004**, *39*, 831–841. [CrossRef]
53. Butler, R.F.; Banerjee, S.K. Theoretical single-domain grain size range in magnetite and titanomagnetite. *J. Geophys. Res.* **1975**, *80*, 4049–4058. [CrossRef]
54. Dunlop, D.J.; Özdemir, O. *Rock Magnetism: Fundamentals and Frontiers*; Cambridge University Press: Cambridge, UK, 1997.
55. Nowaczyk, N.R. Dissolution of titanomagnetite and sulphidization in sediments from Lake Kinneret, Israel. *Geophys. J. Int.* **2011**, *187*, 34–44. [CrossRef]
56. Fabian, K. Thermochemical remanence acquisition in single-domain particle ensembles: A case for possible overestimation of the geomagnetic paleointensity. *Geochem. Geophys. Geosyst.* **2009**, *10*, 1–10. [CrossRef]
57. Shcherbakov, V.P.; Sycheva, N.K.; Gribov, S.K. Experimental and numerical simulation of the acquistion of chemical remanent magnetization and the Thellier procedure. *Izv. Phys. Solid Earth* **2017**, *53*, 645–657. [CrossRef]
58. Gribov, S.K.; Shcherbakov, V.P.; Aphinogenova, N.A. Magnetic properties of artificial CRM created on titanomagnetite-bearing ocean basalts. In *Recent Advances in Rock Magnetism, Environmental Magnetism and Paleomagnetism*; Springer: Berlin/Heidelberg, Germany, 2019; pp. 173–194. [CrossRef]
59. Lightfoot, P.; Keays, R.R.; Doherty, W. Chemical evolution and the origin of nickel sulfide mineralization in the Sudbury Igneous Complex, Ontario, Canada. *Econ. Geol.* **2001**, *96*, 1855–1975. [CrossRef]
60. Robb, L. *Introduction to Ore-Forming Processes*; John Wiley & Sons: Hoboken, NJ, USA, 2020; 496p.
61. Timms, N.E.; Erickson, T.M.; Zanetti, M.R.; Pearce, M.A.; Cayron, C.; Cavosie, A.J.; Reddy, S.M.; Wittmann, A.; Carpenter, P.K. Cubic zirconia in >2370 °C impact melt records Earth's hottest crust. *Earth Planet. Sci. Lett.* **2017**, *477*, 52–58. [CrossRef]

62. Onorato, P.I.K.; Uhlmann, D.R.; Simonds, C.H. The thermal history of the Manicouagan Impact Melt Sheet, Quebec. *J. Geophys. Res. Solid Earth* **1978**, *83*, 2789–2798. [CrossRef]
63. Abramov, O.; Kring, D.A. Numerical modeling of impact-induced hydrothermal activity at the Chicxulub crater. *Meteorit. Planet. Sci.* **2007**, *42*, 93–112. [CrossRef]
64. Warren, P.H.; Claeys, P.; Cedillo-Pardo, E. Mega-impact melt petrology (Chicxulub, Sudbury, and the Moon): Effects of scale and other factors on potential for fractional crystallization and development of cumulates. *Geol. Soc. Am. Spec. Pap.* **1996**, *307*, 105–124.
65. Hildebrand, A.R.; Pilkington, M. Crater-floor exhalative (CRAFEX) sulfide deposits at the Chicxulub crater, Yucatán, México. In Proceedings of the 33rd Lunar and Planetary Science Conference, abstract #2031, Clear Lake, TX, USA, 11–15 March 2002.
66. Wittmann, A.; Expedition 364 Scientists. The mineralogy of the K-Pg transition on the peak ring of the Chicxulub impact crater in drill cores of IODP-ICDP Expedition 364. *Microsc. Microanal.* **2017**, *23*, 2148–2149. [CrossRef]
67. Goderis, S.; Sato, H.; Ferrière, L.; Schmitz, B.; Burney, D.; Kaskes, P.; Vellekoop, J.; Wittmann, A.; Schulz, T.; Chernonozhkin, S.M.; et al. Globally distributed iridium layer preserved within the Chicxulub impact structure. *Sci. Adv.* **2021**, *7*, abe3647. [CrossRef] [PubMed]
68. Pérez-Aguilar, C.D.; Cuéllar-Cruz, M. The formation of crystalline minerals and their role in the origin of life on Earth. *Prog. Cryst. Growth Charact. Mater.* **2022**, *68*, 100558. [CrossRef]
69. Ertem, G. The role of minerals in events that led to the origin of life. *Astrobiology* **2021**, *21*, 137–150. [CrossRef] [PubMed]
70. Brack, A. Clay minerals and the origin of life. *Dev. Clay Sci.* **2013**, *5*, 507–521. [CrossRef]
71. Kloprogge, J.T.; Hartman, H. Clays and the origin of life: The experiments. *Life* **2022**, *12*, 259. [CrossRef]
72. Bernal, J.D. The physical basis of life. *Proc. Phys. Soc. B* **1949**, *62*, 597–618. [CrossRef]
73. Cairns-Smith, A.G. The origin of life and the nature of the primitive gene. *J. Theor. Biol.* **1966**, *10*, 53–88. [CrossRef]
74. Ponnamperuma, C.; Shimoyama, A.; Friebele, E. Clay and the origin of life. *Orig. Life* **1982**, *12*, 9–40. [CrossRef]
75. Meunier, A.; Petit, A.; Cockell, C.S.; Albani, A.E.; Beaufort, D. The Fe-rich clay microsystems in basalt-komatiite lavas: Importance of Fe-smectites for pre-biotic molecule catalysis during the Hadean Eon. *Orig. Life Evol. Biosph.* **2010**, *40*, 253–272. [CrossRef]
76. Bottke, W.F.; Norman, M.D. The Late Heavy Bombardment. *Ann. Rev. Earth Planet. Sci.* **2017**, *45*, 619–647. [CrossRef]
77. Pearson, V.K.; Sephton, M.A.; Kearsley, A.T.; Bland, P.A.; Franchi, I.A.; Gilmour, I. Clay mineral-organic matter relationships in the early solar system. *Meteorit. Planet. Sci.* **2002**, *37*, 1829–1833. [CrossRef]
78. Wächtershäuser, G. Pyrite formation, the first energy source for life: A hypothesis. *Syst. Appl. Microbiol.* **1988**, *10*, 207–210. [CrossRef]
79. Vaughan, D.J.; Lennie, A.R. The iron sulphide minerals: Their chemistry and role in nature. *Sci. Prog.* **1991**, *75*, 371–388.
80. Liu, K.; Huang, F.; Gao, S.; Zhang, Z.; Ren, Y.; An, B. Morphology of framboidal pyrite and its textural evolution: Evidence from the Logatchev area, Mid-Atlantic Ridge. *Ore Geol. Rev.* **2022**, *141*, 104630. [CrossRef]